Mechanism of single-domain selection in epitaxial $CaRuO_3$ thin films

F. Ricci,[1,2,*] M. F. Bevilacqua,[1] F. Miletto Granozio,[1] and U. Scotti di Uccio[1,3]
[1]*Istituto Nazionale Fisica della Materia (INFM), Unità di Napoli, Italy*
[2]*Dip. Scienze Fisiche, Università Federico II di Napoli, Italy*
[3]*Di.M.S.A.T., Università di Cassino, Italy*
(Received 12 October 2001; published 10 April 2002)

$CaRuO_3$ thin films have been grown by on axis sputtering on various (110) $SrTiO_3$, (110) $LaAlO_3$, and (100) $NdGaO_3$ substrates. The growth of high-quality twin free samples, having the *a* axis aligned with the substrate normal, and the *b* and *c* axis aligned with the principal in-plane substrate directions, is demonstrated. The mechanism of domain selection is addressed in terms of free energy minimization during the tetragonal to orthorhombic transition, taking into account both strain and surface energy contributions. On the base of experimental data, it is shown that minimization of surface energy plays a major role in determining film orientation. Obtained samples are especially suited for the investigation of anisotropy in the macroscopic properties of Ca/Sr ruthenates.

DOI: 10.1103/PhysRevB.65.155428 PACS number(s): 68.55.−a

INTRODUCTION

Although several properties of Ru-based distorted perovskites have been studied for many decades, a great surge of interest has occurred in recent years. High-quality samples have been produced both in the form of epitaxial thin films[1] and single crystal, and analyzed from the viewpoint of their structural and electronic properties. As a matter of fact, ruthenates share many fundamental solid-state issues with superconducting cuprates and magnetic manganites, and present in their phase diagram a unique interplay of magnetism and unconventional superconductivity. Furthermore, epitaxial films are employed in prototypes of integrated oxide devices, such as the ones based on superconducting cuprates and/or ferroelectric titanates.

Ru-based complex oxides such as $(Ca,Sr)RuO_3$ and $(Ca,Sr)_2RuO_4$ compounds present structural transitions which lower the symmetry with respect to their high-temperature phase (that is, simple perovskite and K_2NiF_4, respectively). This is attributed to the size of Ca^{2+} and Sr^{2+} ions, which are too small to ''fill'' the space in between RuO_6 octahedra, and thus force Ru-O-Ru bonds to bend in order to reduce the cell volume. Bonds bending, in turn, strongly affects electronic properties by reducing the width of the conduction band. This is believed to determine the different electronic properties in compounds based on the isovalent Ca and Sr ions, since the distortion is greater for the smaller ion (Ca). The dramatic effect of ion size on transport has been also demonstrated by substitution the Ca sites in insulating Ca_2RuO_4 with small amounts of La ions.[2]

In the $CaRuO_3$ and $SrRuO_3$ distorted perovskites, the *buckling* is related to the complex deformation of the structure of RuO_6 octahedra. Upon sample cooling, the octahedra are twisted around the *c* axis during a first phase transition from a cubic perovskite (group 221) to a tetragonal phase (group 140), and then deformed during a second transition to an orthorhombic phase (group 62).[3] In order to investigate the relation between bond bending and transport properties, the growth of twin free samples, exhibiting a single crystallographic orientation, would be highly desirable. In fact, since different bond distortions are present along the different crystallographic directions, and a contribution of twin boundaries to resistivity cannot be ruled out, samples with multiple orientations are unsuitable to detect effects on transport and electronic properties that could be possibly related to strain and to anisotropy. Nevertheless the growth of single oriented thin films does not take place on standard (100) cubic substrates. As discussed in the Appendix, six different crystallographic orientations, all presenting a very similar lattice matching with the cubic substrate, can in principle be expected in $(Ca/Sr)RuO_3$ films. Four of them usually occur, presenting the (110) plane parallel to the substrate. Growth domains with such orientations would differ for the in-plane alignment of the *c* axis and for the possible exchange of *a* and *b* axes.[4,5] Because of symmetry, these four domains are degenerate in energy and therefore nucleate with equal probability. As shown by Gan,[6] such degeneracy can be removed by resorting to a substrate with a vicinal (100) cut, opening the way to the growth of twin-free films. A fully analogous detwinning mechanism has been proved by some of the authors for (110) oriented $YBa_2Cu_3O_7$ thin films.[7] Single-domain (110) $CaRuO_3$ films are nevertheless not optimal for studying the effect of crystalline anisotropy on electronic features (such as transport, magnetic, and optical properties), since principal axes are not aligned in a simple way with respect to substrate. For example, the easy magnetization axis[8,9] of $SrRuO_3$ has been found in such films to be close to the *b* direction, which is at 45° to the substrate normal. Furthermore, the vicinal cut might induce anisotropy in film properties which is not intrinsic, but rather related to the defect structure of the film, as widely demonstrated in HTC superconductors.

In the present work, we report on a systematic study on the structure of high-quality epitaxial $CaRuO_3$ thin films grown on (110) $SrTiO_3$, (110) $LaAlO_3$, and (100) $NdGaO_3$ single crystals. Twin free, purely *a*-axis oriented films are obtained on $SrTiO_3$ and $NdGaO_3$ substrates, while films with mixed *a*-*b* axis orientation are grown on (110) $LaAlO_3$. The mechanism that leads to the selection of domain orientation is discussed in some detail.

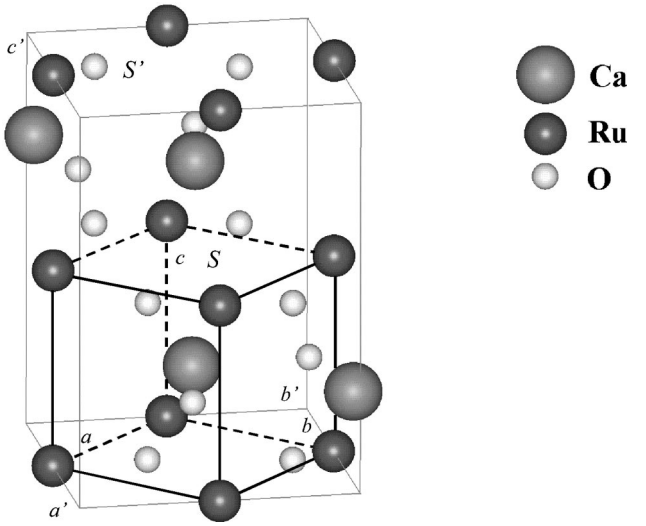

FIG. 1. Sketch showing the geometrical relation between an orthorhombic cell and the parent cubic cell of $CaRuO_3$. In total, six equivalent orthorhombic cells can be build from the same cube.

SAMPLE GROWTH

This work is part of a wider investigation on $CaRuO_3$ deposited in different conditions on substrates of different composition and orientation. The samples were grown by rf magnetron sputtering from a $CaRuO_3$ stoichiometric target. Substrate temperature was typically 700 °C, and gas pressures P_{Ar} and P_{O2} were kept equal and fixed to 6.7 Pa for the samples discussed in this work. (110) $SrTiO_3$ (STO), (110) $LaAlO_3$ (LAO), (100) $NdGaO_3$ (NGO) single crystals were employed as substrates. The three perovskitic substrates present similar in-plane rectangular lattice allowing for epitaxial growth of $CaRuO_3$.

The chemical composition of samples has been analyzed by x-ray photoemission spectroscopy, and discussed in a different paper.[10] The films considered in this paper reproduce the [Ca]:[Ru] 1:1 stoichiometry of the target, and possess excellent transport properties. This is not the case of films grown in identical conditions on the (100) perovskite surfaces, which proved to be Ca-rich and highly resistive.[4]

REMARKS ON DIFFRACTION ANALYSES

The structure of deposited samples was probed by x-ray diffraction (XRD). In addition to performing scans in Bragg-Brentano geometry, a very careful investigation on epitaxy, orientation, strain, and twinning of our $CaRuO_3$ samples was performed, based on reciprocal space mapping (RSM). Details on our experimental apparatus have been reported elsewhere.[7]

$(Ca,Sr)RuO_3$ films are deposited in the cubic phase and become tetragonal and then orthorhombic during cooling.[11] The geometrical relation between the high-temperature cubic cell of the undistorted structure, and the low temperature orthorhombic cell of the distorted structure is shown in Fig. 1. The possible orientations of the orthorhombic cells that can be generated by a (110) oriented cubic unit cell are three: (100), (010), and (112). The total number of possible orthorhombic cells becomes 6, as discussed in the Appendix, if we recognize that four inequivalent variants of (112) orientation exist.

As also shown in the Appendix, (h',k',l') reflections from the orthorhombic $CaRuO_3$ lattice can be divided in two types: (a) those that correspond to lattice planes of the parent cubic cell and (b) those that are generated by the symmetry rupture due to the orthorhombic distortion, and do not exist in the parent cubic structure. When choosing the reflection to investigate in order to distinguish domains with different orientation, both A- and B-type peaks can be chosen: A-peaks generated by different domains, but deriving from the same reflections of the parent cubic cell, fall close to each other in reciprocal space, possibly posing a problem in terms of angular resolution. B-peaks, on the other hand, are typically of much weaker intensity, possibly posing a problem in terms of signal to noise ratio. As an example, in Ref. 6 (221) B-type peaks, possessing a very small intensity (about 10^{-4}, with respect to the strongest reflections) were chosen to assess the single-domain growth of $SrRuO_3$ films. On the other hand, the distortion from the cubic structure in $CaRuO_3$ is larger than in $SrRuO_3$. Therefore, it is easier to resolve correspondent peaks of different film orientations from their position in reciprocal space. For this reason, we decided to investigate $CaRuO_3$ film structure by RSM around peaks of *A* type.

DETERMINATION OF RECIPROCAL SPACE REGIONS TO INVESTIGATE

The relevant regions of reciprocal space were determined by calculation first. Three regions were considered for each sample, in order to achieve a complete description of the unit cell. Two orthogonal cross sections of reciprocal space for epitaxial $CaRuO_3$ films grown on LAO were evaluated and sketched in Figs. 2(a), 2(b). Three possible film orientations, i.e., (100), (010), and (112), are taken into account, according to the above quoted considerations (see also the Appendix). The very small in-plane misalignment between film and substrate reciprocal space vectors ($\Delta\phi < 0.3°$) is neglected in the analysis. This effect is in fact below experimental sensitivity of our x-ray setup, due to the beam angular width perpendicular to the scattering plane. Accordingly, film and substrate reflections are represented in the same reciprocal space cross section. The cross section shown in Fig. 2(a) includes the (110) and (100) reciprocal lattice vectors of LAO, while the cross section shown in Fig. 2(b) includes the (110) and (111) reciprocal lattice vectors of LAO. Only the regions that have been considered in our investigation, that is, in the vicinity of the (330), (400), and (222) substrate reflections, are shown in detail. The presence in each region of a substrate peak is a useful reference for checking the accuracy of measured interplane distances.

Reciprocal space cross sections have been drawn in a similar way for samples deposited on (110) STO, (100) NGO. The case of STO is very similar to LAO. The NGO, instead, is a distorted pervoskite with the same crystal structure as $CaRuO_3$. In particular, (100) NGO substrates are characterized by a (110) oriented parent cubic cell. Reciprocal space mapping was performed in the vicinity of (600),

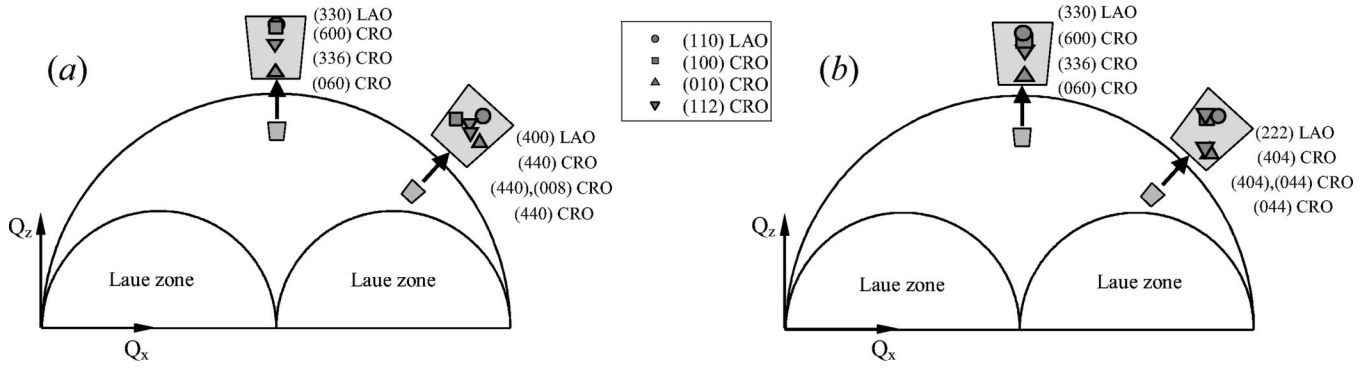

FIG. 2. Sketch of two orthogonal cross sections of reciprocal space for epitaxial $CaRuO_3$ films on $LaAlO_3$.

$(4\bar{4}0)$, and $(40\bar{4})$ reflections, that correspond, according to the Appendix, to the (330), (400), and (222) reflections of the cubic cell.

The expected interplane distances relative to all substrate and film peaks considered in this work are reported in Table I. The calculation is based on the bulk value of lattice spacing. For each substrate, the three orientations of the $CaRuO_3$ cell discussed above are considered. The four possible variants of the (112) orientation result in different interplane distances in the asymmetric reflections. Comparison of experimental results with these calculated data allowed a straightforward determination of orientation and strain in our samples. Notice that symmetric peaks detection leads to univocal identification of the $CaRuO_3$ domains orientation, since the difference of interplane distances are large with respect to experimental accuracy.

RESULTS

θ-2θ scans performed on three samples, respectively, deposited on (110) STO, (110) LAO, and (100) NGO are reported in Figs. 3(a)–3(c). Reported Miller indexes for the different reflections have been assigned according to the considerations reported above. Diffraction patterns are indicative of samples with high crystal quality. The width of symmetrical rocking curves, typically ranging between 0.16° and 0.33°, are typical of high quality oxide films.

RSM of films deposited on (110) STO, (110) LAO, and (100) NGO are, respectively, reported in Figs. 4, 5, and 6. Due to the 2θ angular width of film peaks, an average wavelength value $\lambda = 0.154187$ nm for the Cu$K\alpha$ radiation was employed to determine the Q_x, Q_z values for $CaRuO_3$ (Table II) and to plot the reciprocal space maps. The Cu$K\alpha_1$-Cu$K\alpha_2$ splitting was instead properly taken into account in the determination of substrate lattice parameters. The values of measured lattice parameters of films and substrates are summarized in Table III.

$CaRuO_3$ films on STO substrates. Maps performed in the vicinity of the (330), (400), and (222) substrate peaks, for $CaRuO_3$ thin films deposited on (110) STO are, respectively, reported in Figs. 4(a)–4(c). The value of the perpendicular lattice spacing $d = 0.0896$ nm proves that $CaRuO_3$ is single-domain, *a*-axis oriented.

The following epitaxial relations are observed: (100) $CaRuO_3 \| (110)$ STO; (010) $CaRuO_3 \| (1\bar{1}0)$ STO; (001) $CaRuO_3 \| (001)$ STO. Due to the parallelism of $CaRuO_3$ and substrate axes, the Q_x, Q_z maps allow one to quickly correlate the experimental results to the interplane distances and lattice parameters of the sample. The lattice spacing perpendicular to the substrate plane (d_{out}) is determined in symmetric reflections, as $d_{out} = 2\pi/Q_z$. Both the out-of-plane (d_{out}) and one of the in plane in-plane (d_{in}) film lattice spacing are determined in our asymmetric reflections ($d_{out} = 2\pi/Q_z, d_{in} = 2\pi/Q_x$). Therefore, the mapping of one symmetric and two asymmetric peaks provides redundant data on lattice parameters, which resulted to be consistent within experimental error. Similar considerations also apply to the other reported measurements.

TABLE I. Expected interplane distances relative to the substrate and film reflections addressed in this work. Reported values are calculated on the base of bulk lattice parameters.

Crystal orientation or growth domain		Symmetric reflection	d (pm)	First asymmetric reflection	d (pm)	Second asymmetric reflection	d (pm)
LAO	(110)	(330)	89.40	(400)	94.83	(222)	109.5
STO	(110)	(330)	92.04	(400)	97.63	(222)	112.7
NGO	(100)	(600)	90.43	(440)	96.53	(404)	110.9
	(100)	(600)	89.33	(440)	96.22	(404)	109.8
CRO	(010)	(060)	92.17	(440)	96.22	(044)	112.1
	(112)	(336)	90.49	(008), (440)	95.75, 96.22	(404) (044)	109.8, 112.1

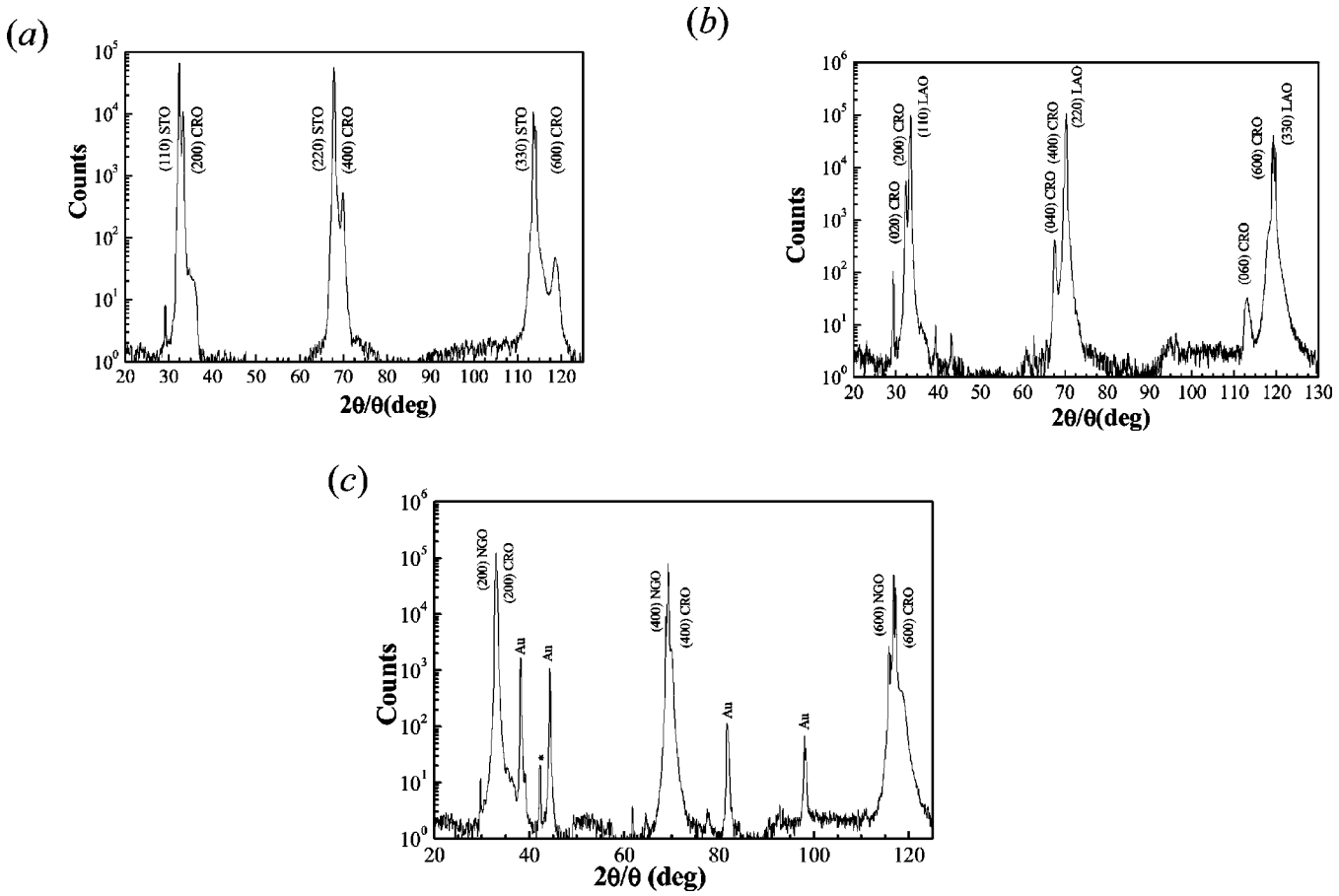

FIG. 3. θ-2θ scans for CRO films grown on (a) (110) $SrTiO_3$, (b) (110) $LaAlO_3$, and (c) (100) $NdGaO_3$ substrate. Au peaks in (c) are due to contacts deposited for transport measurements. Reflection peak labeled with * is due to unfiltered $K\beta$ radiation.

$CaRuO_3$ films on LAO substrates. At difference to the case of films deposited on the other substrates, the growth orientation of $CaRuO_3$ on (110) LAO may differ from sample to sample. RSM performed in the vicinity of the (330), (400), and (222) LAO reflections for one of our samples are, respectively, reported in Figs. 5(a)–5(c). The presence of two distinct film orientations is recognized in this case. The interplane distances $d=0.0896$ nm, $d'=0.0921$ nm deduced from the symmetric reflections [Fig. 5(a)] allow one to unambiguously single out the presence of both *a*-axis and *b*-axis oriented $CaRuO_3$. An estimate of the relative amount of the two domains can be obtained on the base of Fig. 5(b). Here peaks relative to different domains, but corresponding to the same Miller indexes (440), are shown. On then base of the ratio of the integrated intensities, a relative amount of *a*-axis orientation $F_a=0.51$ can be inferred for the considered sample.

The complete analysis of results from symmetric and asymmetric reflections is reported in Table II. The epitaxial relations are the following: *a*-axis domain: (100) $CaRuO_3 \| (110)$ LAO, (010) $CaRuO_3 \| (1\bar{1}0)$ LAO, (001) $CaRuO_3 \| (001)$ LAO; *b*-axis domain: (010) $CaRuO_3 \| (110)$ LAO, (100) $CaRuO_3 \| (110)$ LAO, (001) $CaRuO_3 \| (001)$ LAO. The corresponding in-plane lattice parameters are reported in Table III.

Other samples deposited on (110) LAO grew instead with pure *a*-axis orientations. RS maps were substantially similar to those in Fig. 4, and are not reported here. The dependence of the orientation ratio among *a*-axis and *b*-axis orientation on deposition conditions is not addressed in this work. We just mention that no samples with higher *b*-axis content, with respect to the sample in Fig. 5, were obtained.

$CaRuO_3$ films on NGO substrates. Maps performed in the vicinity of the (600), (440), and (404) substrate peaks, for $CaRuO_3$ thin films deposited on (100) NGO are, respectively, reported in Figs. 6(a)–6(c). From the value of the perpendicular lattice parameter, the film is determined as *a*-axis oriented. The $CaRuO_3$ principal axes are aligned with the corresponding substrate directions (100) $CaRuO_3 \| (100)$ NGO, (010) $CaRuO_3 \| (010)$ NGO, (001) $CaRuO_3 \| (001)$ NGO. Once again, the obtained values for Q_x, Q_z, and the Q modulus are reported in Table II, while values for the lattice parameters are reported in Table III.

Film transport properties. $R(T)$ plots were obtained for a number of several single-domain, *a*-axis samples grown on different substrates. Room-temperature resistivities were determined on unpatterned films by the van der Pauw method. All samples showed similar plots, with room temperature resistivities varying in the range 230–360 $\mu\Omega$ cm, and a resistive ratio R_{300}/R_0 in between 2 and 3. The $R(T)$ plot for one of the samples, a single-domain, *a*-axis oriented $CaRuO_3$ film grown on (110) LAO, is shown in Fig. 7. The room-

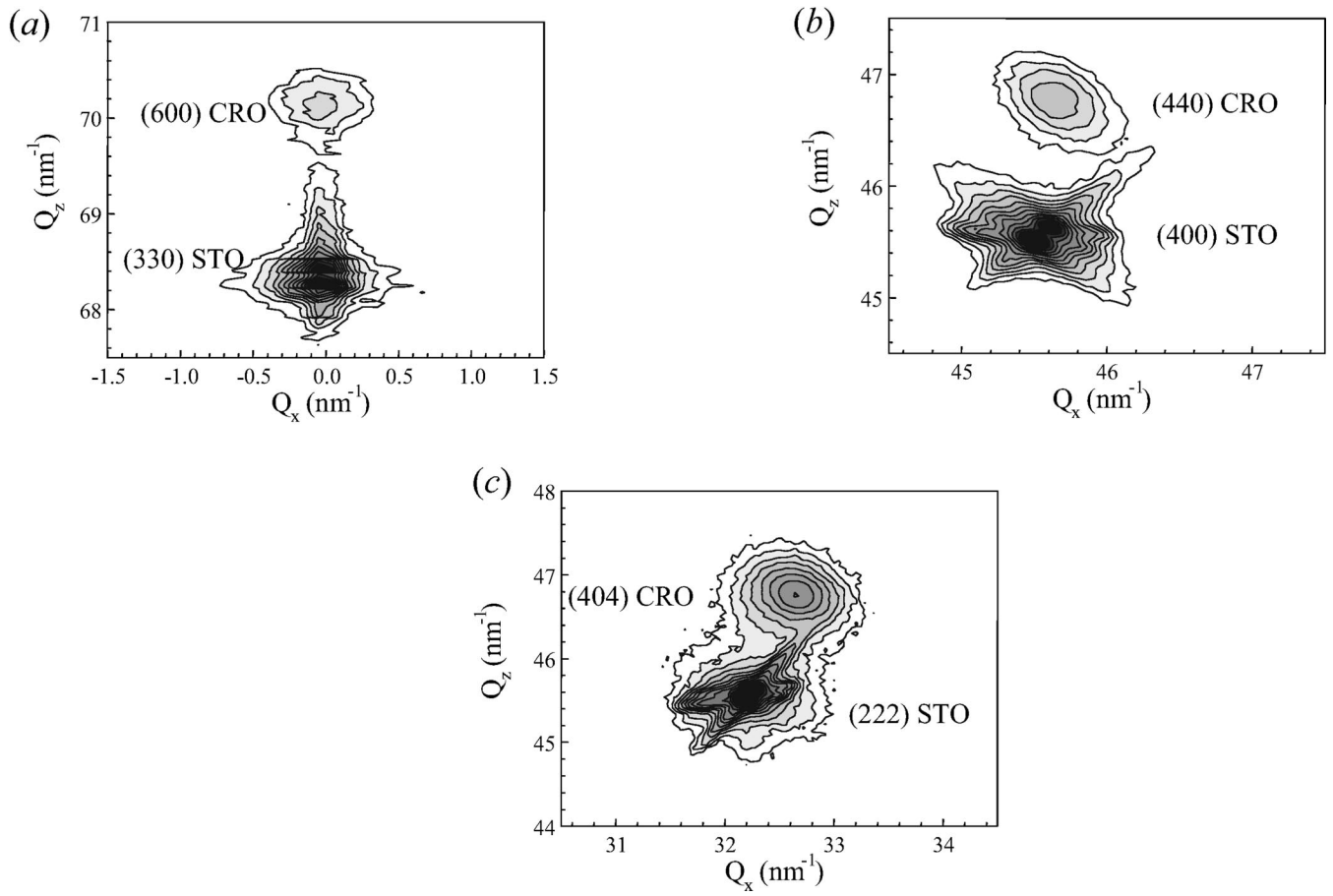

FIG. 4. Maps of different regions of the reciprocal space of a CRO film grown onto a (110) STO substrate: (a) map around the (330) STO peak; (b) map around the (400) STO peak; (c) map around the (222) STO peak.

temperature resistivity is $\rho_{300}=360\ \mu\Omega$ cm, and the resistivity ratio is $R_{300}/R_0=2.18$. The peculiar nonlinear low-temperature and high-temperature behavior of $CaRuO_3$ resistivity vs temperature, also evident in our sample, has been interpreted by some authors as a signature of non-Fermi-liquid behavior.[12] No clear correlation of the resistive behavior with substrate type, within the class of substrates considered in this work, was found in our plots. We notice that under the same deposition conditions, films grown on (100) STO, (100) LAO, and (110) NGO are instead characterized by higher values of resistivity and semiconducting behavior, as discussed in a separate paper.[10]

DISCUSSION

Among the six possible variants of lattice matched growth orientations that can be expected for $CaRuO_3$ on (110) perovskites, only two exhibiting either the *a* or the *b* axis along the growth direction were found. In the following, the competition between such growth orientations is discussed.

The formation of *a*-axis or of *b*-axis domains takes place during cooling,[11] rather than during the deposition stage. Therefore, this phenomenon is not related to the growth kinetics of impinging atoms. Having ruled out kinetic effects, we conclude that the domain orientation is determined by thermodynamics, that is, by free energy minimization. By assuming that entropy related terms are only weekly dependent on orientation, the energetic balance is mainly determined by the potential energy *U*. The energy balance of a two-dimensional crystal layer epitaxially grown on a single crystal substrate is reviewed in the following.

Let us write *U* as

$$U=(u_0+u_e)V+u_s^{fv}S+u_s^{fs}S, \tag{1}$$

where u_0 is the condensation energy per unit volume of the $CaRuO_3$ crystal with respect to a conventional zero energy state (e.g., the state where all atoms constituting the crystal are at infinity), u_e is the elastic energy related to the strain, and hence to film-substrate lattice mismatch, u_s^{fv} is the surface energy related to the film-vacuum interface on the upper side of the film, and u_s^{fs} is the surface energy related to the film-substrate interface on the lower side of the film. In epitaxial films $u_s^{fv}>u_s^{fs}$. In fact, the film-vapor interface is characterized by dangling bonds, which are instead mostly saturated at the film-substrate interface, if the two lattices are similar enough.

The role of surface energy is very relevant when discussing film growth issues, although often not properly taken into account. For example, some of the authors have shown that

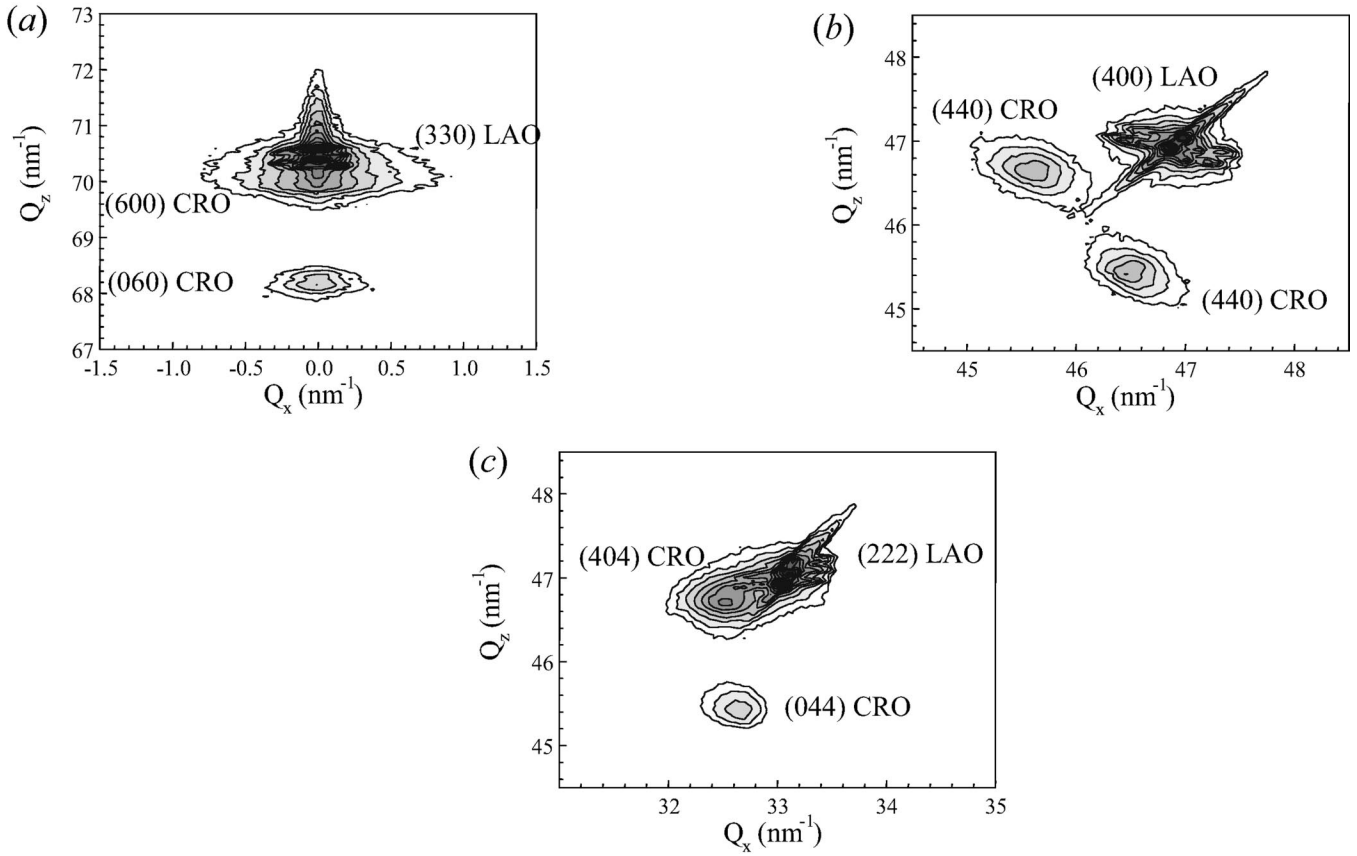

FIG. 5. Maps of different regions of the reciprocal space of CRO grown onto a (110) LAO substrate: (a) map around the (330) LAO peak; (b) map around the (400) LAO peak; (c) map around the (222) LAO peak.

in $YBa_2Cu_3O_7$ anisotropy of surface energies, rather than minimization of strain, is fundamental both in determining the unit cell orientation (in the high-temperature tetragonal phase) and the relative orientation of *a*-*b* axes (during the cooling to the orthorhombic phase).[7,13] In the case of $CaRuO_3$, the anisotropy of surface energies is expected to be smaller with respect to $YBa_2Cu_3O_7$. In fact, while (100), (010), and (001) $YBa_2Cu_3O_7$ lattice planes have different chemical compositions, (100), (010), and (001) $CaRuO_3$ planes are only topologically different. Nevertheless, we argue that surface energy anisotropy is relevant to $CaRuO_3$ film orientation, and that the minimization of strain (and hence of lattice mismatch) cannot account for the phenomenology described in this work. In order to prove this statement, simple misfit evaluations based on bulk $CaRuO_3$ lattice parameters are presented in the following to comment on our experimental evidence.

In the case of (110) STO substrate, minimization of lattice mismatch tends to favor *a*-axis growth with respect to *b*-axis growth. In fact, the in-plane lattice parameter in the $(1\bar{1}0)$ STO direction fits the *b* axis of bulk $CaRuO_3$ with a much lower mismatch ($\sim$0.1%) with respect to the *a* axis ($\sim -2.9\%$). As a matter of fact, purely *a*-axis orientation is found.

a-axis growth is favored by minimization of lattice mismatch also on the (100) NGO substrates. The in-plane (010) NGO lattice parameter fits in fact the *b* axis of bulk $CaRuO_3$ with a lower mismatch ($\sim$0.6%) with respect to the *a* axis ($\sim -2.5\%$). Furthermore NGO presents the same distorted structure of $CaRuO_3$. The (100) oriented $CaRuO_3$ keeps the same distortion of octahedra, and thus similar atomic positions, across the film-substrate interface. This obviously allows one to minimize lattice disorder at the film-substrate interface, and thus minimize the u_s^{fs} energy term. Data about STO and $NdGaO_3$ alone would not be in contrast with a picture in which orientation is only determined by strain minimization.

On the other hand, the case of LAO is completely different. In fact, minimization of lattice mismatch would clearly tend to favor *b*-axis growth. The *a* axis of bulk $CaRuO_3$ (mismatch below 0.1%) fits the $(1\bar{1}0)$ LAO spacing well. The $CaRuO_3$ *b* axis, on the other hand, has a large misfit ($\sim$3.2%). However, we did not succeed in growing pure *b*-axis $CaRuO_3$ films on LAO. On the contrary, pure *a*-axis films may be achieved. A comparable amount of both orientations has also been observed in some samples, proving that competing mechanisms act in this case.

Looking at the values of the in-plane lattice parameters of *a*-axis $CaRuO_3$ domains grown on LAO, we notice that a considerable strain relief takes place probably due to lattice dislocations close to the substrate plane. Accordingly, we expect that the elastic energy contribution u_e is small in this case. On the other hand, dislocations formation has an energy cost that increase the u_s^{fs} term in Eq. (1). Thus, we

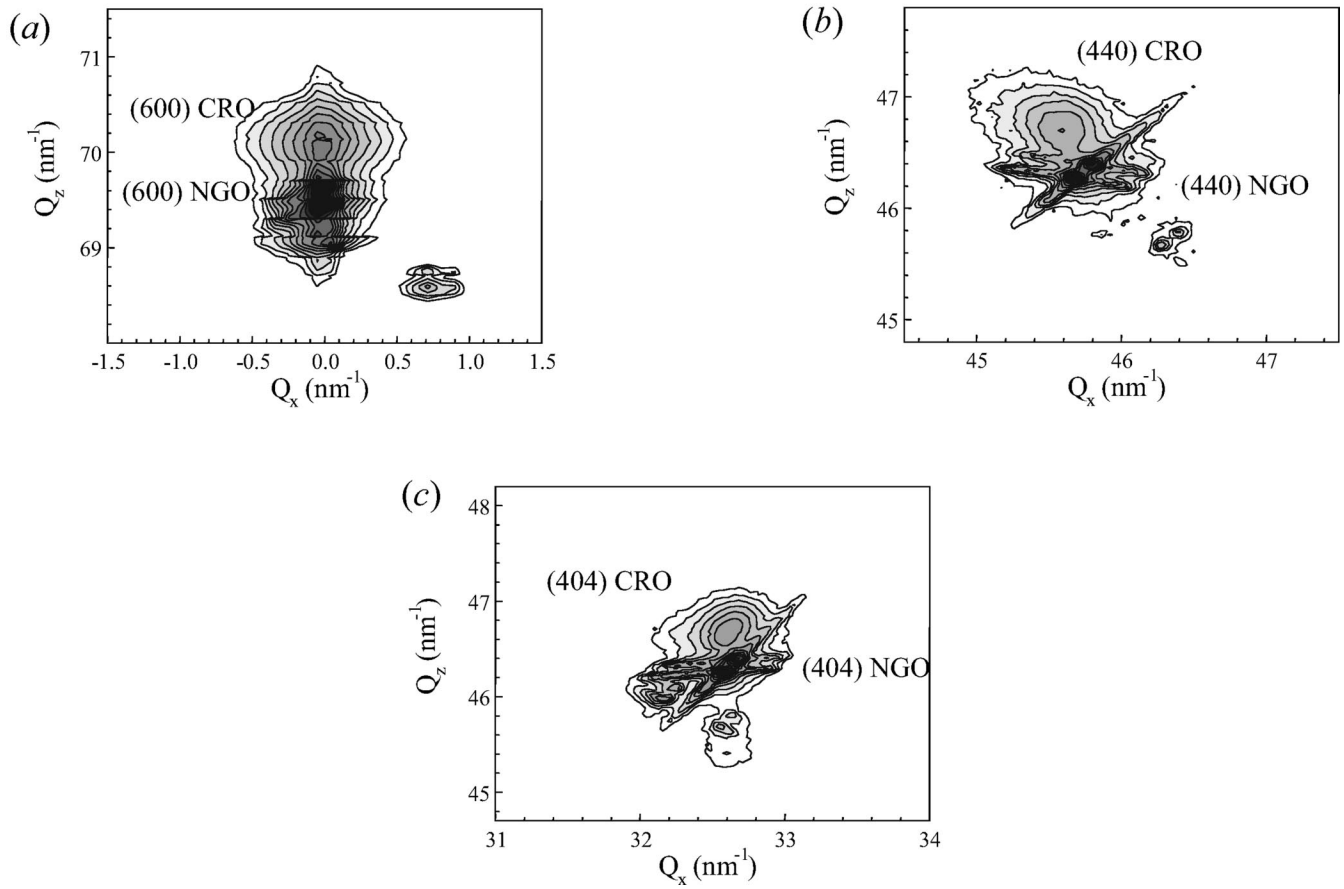

FIG. 6. Maps of different regions of the reciprocal space of CRO grown onto (100) NGO: (a) map around the (600) NGO peak; (b) map around the (440) NGO peak; (c) map around the (404) NGO peak.

realize that the energy gain that is obtained by selecting *a*-axis growth with respect to *b*-axis growth depends on the u_s^{fv} term. In other terms, the surface energy of $CaRuO_3$ (100) facets must be sensitively lower than the surface energy of (010) facets. The difference must be large enough, to compensate the energy spent in dislocation formation.

The fact that $CaRuO_3$ (100) facets have lower surface energy can be qualitatively understood on the base of a relatively crude argument. At high-temperature $CaRuO_3$ is cubic, and the directions corresponding to the orthorhombic *a* axis and *b* axis are equivalent. Upon cooling, the *a*-axis facets are expanded, while the *b*-axis facets are compressed. Roughly, we can imagine that the surface energy is related to the dangling bonds that are obtained, when a surface is created by breaking apart a crystal along a given crystallographic plane. Let us neglect the variation of bond energies due to the different atomic rearrangements. As the same kind of dangling bonds are obtained along cuts parallel to (100) or to (010) facets, the ratio of surface energies grossly corresponds to the ratio of bond densities. During the tetragonal to orthorhombic transition, the number of bonds remains constant, but the surface density changes because (100) surfaces expand, and (010) surfaces shrink. In general, if the surface S varies by an amount ΔS:

$$\Delta(u_s^{fv}S) = u_s^{fv}\Delta S + \Delta u_s^{fv} S = 0. \tag{2}$$

The surface energy of the film-vapor interface after the transition u'^{fv}_s is related to u_s^{fv} before the transition by the relation

$$u'^{fv}_s = u_s^{fv}\left(1 - \frac{\Delta S}{S}\right). \tag{3}$$

Equation (3) proves that the lower surface energy per unit area must correspond to the larger facet area, that is an *a* facet. A surface energy difference of ~3% may be inferred by this model.

CONCLUSIONS

We have grown high-quality $CaRuO_3$ films on (110) STO, (100) NGO, and (110) LAO substrates by rf sputtering. The samples deposited on perovskitic substrates are epitaxial and present excellent transport properties. Our attention has been focused on the study of the crystallographic orientation of the films and on the domain orientation selection. Our data demonstrate that single-domain, *a*-axis $CaRuO_3$ films are obtained on (110) STO, (100) NGO, and (110) LAO. Mixed *a*-axis and *b*-axis domains can only develop in specific conditions on (110) LAO.

The possibility to achieve single-domain $CaRuO_3$ results in high-quality samples, with respect to both crystallographic

TABLE II. Experimental values extracted from RS maps, performed on CRO films deposited on (110) STO, (110) LAO, and (100) NGO substrates and, respectively, reported in Figs. 4, 5, and 6. For each analyzed diffraction peak, measured values for the Q_x, Q_z components of the scattering vectors and interplane distances are reported.

Substrate	Peak	Q_x (nm^{-1})	Q_z (nm^{-1})	d (pm)
	(330) STO	0.00	68.25	92.06
	(600) CRO	0.0	70.2	89.6
(110) STO	(400) STO	45.51	45.52	97.62
	(440) CRO *a* axis	45.7	46.7	96.2
	(222) STO	32.18	45.52	112.71
	(404) CRO *a* axis	32.7	46.8	110.2
	(330) LAO	0.00	70.36	89.30
	(600) CRO	0.0	70.1	89.6
	(060) CRO	0.0	68.2	92.1
	(400) LAO	46.87	46.92	94.74
(110) LAO	(440) CRO *a* axis	45.6	46.7	96.3
	(440) CRO *b* axis	46.5	45.4	96.6
	(222) LAO	33.08	46.99	109.34
	(404) CRO *a* axis	32.6	46.7	110.3
	(044) CRO *b* axis	32.5	45.4	112.5
	(600) NGO	0.00	69.47	90.44
	(600) CRO	0.0	70.0	89.7
(100) NGO	(440) NGO	45.72	46.31	96.55
	(440) CRO *a* axis	45.6	46.7	96.2
	(404) NGO	32.61	46.31	110.93
	(404) CRO *a* axis	32.6	46.7	110.3

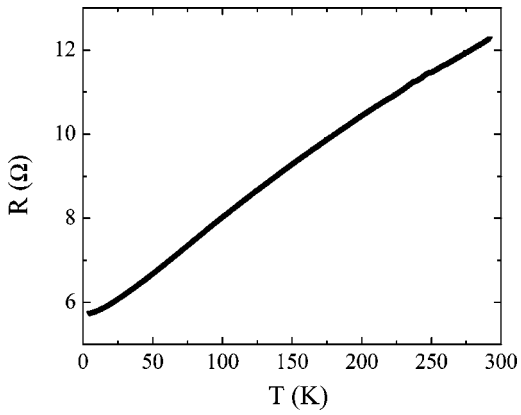

FIG. 7. $R(T)$ plot for a single domain, *a*-axis oriented CRO film grown on (110) LAO.

and transport properties. Single-domain formation is the result of the growth process, that can be divided into two parts. During the film deposition at high temperature, $CaRuO_3$ is cubic. During the cooling process, the film undergoes a double structural transition, so that at room temperature it is in the orthorhombic form. In this work, we addressed the problem of the orientation of the domains during this last step. This process takes place close to the thermodynamical equilibrium, and therefore is driven by Gibbs energy minimization. In this framework, we have shown that the selection of the *a*-axis orientation can be understood on the basis of simple considerations on the surface energy of orthorhombic $CaRuO_3$.

TABLE III. Experimental values extracted from RS maps, performed on CRO films deposited on (110) STO, (110) LAO, and (100) NGO substrates and respectively, reported in Figs. 4, 5, and 6. Lattice parameters a_i^f $(i=1,2,3)$ for the obtained growth orientations of the CRO film are reported, and compared with bulk values ($a_i^b, i=1,2,3$) and corresponding substrate in-plane lattice spacing d_i^s. For each case, obtained values of strain, lattice mismatch with substrate and relative volume variation are reported.

Substrate	Growth orientation	CRO lattice parameters a_i^f (nm)		Strain $\frac{a_i^f}{a_i^b}-1$	Mismatch with substrate $\frac{a_i^f}{d_i^s}-1$	Volume variation $\frac{V^f}{V^b}-1$
LAO		*a*	0.5377	0.3%		
	a axis	*b*	0.5510	−0.4%	2.8%	0.5%
		c	0.770	0.5%	1.6%	
		a	0.5528	0.8%	0.9%	
	b axis	*b*	0.5405	0.0%		1.7%
		c	0.773	0.9%	2%	
		a	0.5374	0.3%		
STO	*a* axis	*b*	0.5505	−0.4%	−0.3%	0.3%
		c	0.770	0.5%	−1.5%	
		a	0.5383	0.4%		
NGO	*a* axis	*b*	0.5509	−0.4%	0.2%	0.6%
		c	0.770	0.5%	−0.1%	

APPENDIX

Ca/Sr ruthenate films are cubic during deposition,[11] and their epitaxy is ''cube on cube'' on usual perovskitic substrates. In order to gain an intuitive understanding about the different possible orientations of the orthorhombic cell that can develop during cooling, it is important to stress out the relation between the parent cubic cell and the orthorhombic one (Fig. 1). For diffraction analyses, it is also useful to find the algebraic equations relating the indices of a given plane in cubic notation, with the indices of the corresponding planes, in orthorhombic notation. This issue is briefly addressed in the following.

Consider a perovskite structure, representing the high-temperature phase of Ca/Sr ruthenate (being orthorhombic at room temperature, space group 62). Define as usually a cubic unit cell by assigning a right-handed triplet S of Cartesian axes (a, b, c) to its principal directions. As a possible nonunit elementary cell, with lower symmetry, we can define in this lattice a tetragonal unit cell with volume $4a^3$, determined by a right-handed triplet of axes $S'(a',b',c')$ as shown in Fig. 1. At room temperature S no more represents a unit cell, while S' (though distorted to orthorhombic) remains as the unit, highest symmetry, cell of the lattice.

Back to the cubic lattice, it is recognized that the number of different S' cells that can be defined is 6. Each of them can be characterized on the base of the following properties: (1) having the c' axis parallel to a, b, or c and (2) being right or left handed. Accordingly, they can be itemized as S'_{ra}, S'_{la}, S'_{rb}, S'_{lb}, S'_{rc}, S'_{lc}. For example, S'_{ra} is a right-handed triplet having the c' axis parallel to the a axis of S.

Define the Miller indices of a given crystal plane relative to the S triplet as (h, k, l) and (h',k',l') its Miller indices relative to the S' triplet. The algebraic relations that relate the Miller indices of the S cell and of each of the six S'_{ij} cells are reported in Table IV. They are derived from the geometrical relations between the cubic and orthorhombic cell, and can be easily understood by inspection.

Equations in Table IV tell us that from a cubic film presenting the (100) plane parallel to the substrate plane, the following orientations can be obtained after cooling for the orthorhombic cells: (110), $(1\bar{1}0)$, and (001). Each of them can occur with two different in-plane orientation, thus yielding a total of 6. From a (110) cubic film, the following orientations are obtained instead: (100), (010), and (112). (112) can occur with four different in-plane orientations.

TABLE IV. For any of the six possible orthorhombic cells generated by the same parent cubic cell, the transformation law between indices (h',k',l') and (h, k, l) is reported. In the upper part, (h',k',l') indices for a given plane are expressed in term of the Miller indices (h, k, l) of the same plane in cubic notation. The inverse transformation is reported in the lower part.

	h'	k'	l'
S'_{rc}	$h+k$	$h-k$	$2l$
S'_{lc}	$h-k$	$h+k$	$2l$
S'_{ra}	$k+l$	$k-l$	$2h$
S'_{la}	$k-l$	$k+l$	$2h$
S'_{rb}	$l+h$	$l-h$	$2k$
S'_{lb}	$l-h$	$l+h$	$2k$
	h	k	l
S'_{rc}	$(h'+k')/2$	$(h'-k')/2$	$l'/2$
S'_{lc}	$(h'+k')/2$	$-(h'+k')/2$	$l'/2$
S'_{ra}	$(k'+l')/2$	$(k'-l')/2$	$h'/2$
S'_{la}	$(k'-l')/2$	$-(k'+l')/2$	$h'/2$
S'_{rb}	$(l'+h')/2$	$(l'-h')/2$	$k'/2$
S'_{lb}	$(l'-h')/2$	$-(l'+h')/2$	$k'/2$

Note that not all the (h',k',l') triplets correspond to an integer (h,k,l) triplet. For this to happen, l' needs to be even, and (h,k) to have the same parity. (h',k',l') triplets not corresponding to a (h,k,l) triplet in cubic notation, have associated no diffracted intensity in the high-temperature cubic phase. Under the transition temperatures to the tetragonal and then to the orthorhombic phase, some of them might have associated a diffracted intensity, as a result of symmetry rupture. An example is given by the (221) peak, employed in diffraction analysis in Ref. 14. Other reflections are instead still forbidden for symmetry reasons.

ACKNOWLEDGMENTS

The authors wish to acknowledge support provided by the Consiglio Nazionale delle Ricerche under the Progetto Finalizzato ''Cluster, strati sottili, e particelle per impieghi magnetici.''

*Present address: Pirelli Labs, viale Sarca 222, 20126 Milano, Italy.

[1] C. B. Eom, E. J. Cava, R. M. Fleming, Julia M. Phillips, R. B. van Dover, J. H. Marshall, J. W. P. Hsu, J. J. Krajewski, and W. F. Peck, Science **258**, 1766 (1992).

[2] G. Cao, S. McCall, V. Dobrosavljevic, C. S. Alexander, J. E. Crow, and R. P. Guertin, Phys. Rev. B **61**, R5053 (2000).

[3] M. Braden, G. André, S. Nakatsuji, and Y. Maeno, Phys. Rev. B **58**, 847 (1998).

[4] Different notations are sometimes employed for the a, b, and c lattice parameters. We will resort to the most natural notation, where a is the shortest and c the longest axis. For $CaRuO_3$: $a = 0.536$ nm, $b = 0.553$ nm, $c = 0.766$ nm.

[5] J. C. Jiang, W. Tian, X. Q. Pan, Q. Gan, and C. B. Eom, Appl. Phys. Lett. **72**, 2963 (1998).

[6] Q. Gan, R. A. Rao, and C. B. Eom, Appl. Phys. Lett. **70**, 1962 (1997).

[7] F. Miletto Granozio, F. Ricci, U. Scotti di Uccio, and J. C. Villegier, Phys. Rev. B **57**, 6173 (1998).

[8] Q. Gan, R. A. Rao, C. B. Eom, L. Wu, and F. Tsui, J. Appl. Phys. **85**, 5297 (1999).

[9] L. Klein, J. S. Dodge, C. H. Ahn, J. W. Reiner, L. Mieville, T. H. Geballe, M. R. Beasley, and A. Kapitulnik, J. Phys.: Condens. Matter **8**, 10 111 (1996).

[10] F. Miletto Granozio, F. Bevilacqua, G. G. Condorelli, F. Ricci, and U. Scotti di Uccio (unpublished).

[11] Jon-Paul Maria, H. L. McKinstry, and S. Trolier-McKinstry, Appl. Phys. Lett. **76**, 3382 (2000).

[12] Kostic, Y. Okada, N. C. Collins, Z. Schlesinger, J. W. Reiner, L. Klein, A. Kapitulnik, T. H. Geballe, and M. R. Beasley, Phys. Rev. Lett. **81**, 2498 (1998).

[13] F. Miletto Granozio, U. Scotti di Uccio, M. Salluzzo, I. Maggio-Aprile, and Ø. Fischer, Phys. Rev. B **61**, 756 (2000); F. Miletto Granozio and U. Scotti di Uccio, J. Cryst. Growth **174**, 409 (1997).

[14] Q. Gan, R. A. Rao, and C. B. Eom, Appl. Phys. Lett. **70**, 1962 (1997).